

Odd-Parity Nucleon Electromagnetic Transitions in Lattice QCD

Finn M. Stokes,^{1,2} Benjamin J. Owen,^{1,*} Waseem Kamleh,¹ and Derek B. Leinweber¹

¹*Special Research Centre for the Subatomic Structure of Matter,
Department of Physics, University of Adelaide, South Australia 5005, Australia*

²*Jülich Supercomputing Centre, Institute for Advanced Simulation,
Forschungszentrum Jülich, Jülich D-52425, Germany*

The parity-expanded variational analysis (PEVA) technique enables the isolation of opposite-parity eigenstates at finite momentum. The approach has been used to perform the first lattice QCD calculations of excited-baryon form factors. In particular, these calculations show that the low-lying odd-parity nucleon excitations are described well by constituent quark models at moderate u and d quark masses approaching the strange quark mass. Herein, we extend the PEVA technique to establish a formalism for the determination of odd-parity nucleon electromagnetic transition form factors in lattice QCD. The formalism is implemented in the first calculation of the helicity amplitudes for transitions from the ground state nucleon to the first two odd-parity excitations. Through a comparison with constituent quark model calculations of these amplitudes, these new results give important insight into the structure of these excitations. This work is a critical step towards confronting experimental electroproduction amplitudes for the $N^*(1535)$ and $N^*(1650)$ resonances with *ab-initio* lattice QCD calculations.

I. INTRODUCTION

The study of nucleon resonances is a challenging and rich field. The structure of such states can be probed experimentally through meson electroproduction. Such measurements of nucleon resonance electrocouplings have existed for over a decade, but have yet to be confronted with *ab-initio* calculations.

Lattice QCD studies of resonance electrocouplings provide not only the opportunity to confront experiment, but can also provide important insight into the nature of baryon excitations and the manner in which their structure changes as the quark masses take values away from the physical regime. Through a comparison with model calculations, one can learn the veracity of the model and gain insight into the manner in which QCD gives rise to the observed phenomena.

This approach has already emphasised how low-lying odd-parity nucleons are described well by constituent quark models when the light-quark masses in the simulations take moderate values approaching the strange quark mass [1–4]. This finding is driving new extensions of Hamiltonian effective field theory (HEFT) calculations [5–11] where two bare-baryon basis states are incorporated in a coupled-channel analysis of S_{11} pion-nucleon scattering [12, 13].

Computing the electrocouplings of physical resonances from lattice QCD is a challenging and multifaceted endeavour that requires a number of problems to be solved. First, a formalism for the determination of odd-parity nucleon electromagnetic transition form factors in lattice QCD needs to be established. This is the focus of the present investigation. Here the parity-expanded variational analysis (PEVA) technique [1, 14, 15] is essential to the isolation of baryon eigenstates at finite momentum.

Subsequently, contributions from multi-particle scattering states need to be understood. This will require the use of non-local momentum-projected meson-baryon operators and excellent progress is being made for two-point functions relevant to the mass spectrum [16–23]. The calculation of scattering-state contributions to baryon three-point functions relevant to matrix elements has yet to be considered. Once the matrix elements are determined on the lattice, one must draw on a formalism to connect the finite-volume calculations to the infinite-volume resonances in nature. Here scattering state contributions will play a nontrivial role.

In this light, the study presented here focuses on the matrix elements of low-lying energy eigenstates at larger quark masses where the states dominated by single-particle operators are the lowest-lying states in the finite-volume spectrum. Our aim is to establish a formalism in lattice QCD for the determination of odd-parity nucleon electromagnetic transition form factors and illustrate the formalism in practice through first calculations of the helicity amplitudes for transitions from the ground state nucleon to the first two odd-parity excitations.

As such, our comparison is not with experiment, but rather with constituent quark-model calculations of these amplitudes to gain insight into the veracity of these early model calculations [24]. We are keen to learn if the success of the quark model in capturing the essence of the physics for both ground state and odd-parity excited-state magnetic moments of the nucleon is realised for electromagnetic transitions between these states. Here, nontrivial momentum dependencies introduce new challenges for the quark model.

Thus, this investigation focuses on the problem of accessing the relevant matrix elements in lattice QCD and the need for careful regard to state isolation and opposite-parity contaminations. Establishing this formalism is a critical step towards confronting experimental electroproduction amplitudes for the $N^*(1535)$ and $N^*(1650)$ res-

* Now at the Bureau of Meteorology, Adelaide, SA, Australia.

onances with *ab-initio* lattice QCD calculations.

It has been well-established that variational analysis techniques provide a powerful tool for isolating individual states in lattice QCD [25, 26]. However, conventional variational analyses have relied upon a naive zero-momentum parity projection which fails at finite momentum. The recent introduction and application of the parity-expanded variational analysis (PEVA) technique [1, 14, 15] offers a solution to this problem. By extending a conventional variational analysis, both odd and even-parity baryon eigenstates can be simultaneously isolated at finite momentum. In this paper, we extend this technique to the calculation of transition form factors of baryons.

Section II commences with a review of the covariant vertex functions for both positive and negative parity transition matrix elements and outlines the relationship between the associated form factors and the helicity amplitudes of experimental interest. Here we introduce a new formalism and discuss its relative merits. Section III briefly reviews the PEVA technique and outlines its application to odd-parity electromagnetic transitions between the nucleon ground state and odd-parity excitations of the nucleon. Finally, the formalism is applied to calculate the odd-parity nucleon resonance electrocouplings and the results are compared with legacy quark-model calculations in Sec. IV. Section V concludes our presentation with a summary.

II. COVARIANT VERTEX FUNCTIONS AND HELICITY AMPLITUDES

In our previous work [1], we made use of variational techniques to evaluate the elastic electromagnetic form factors for the lightest negative-parity nucleon states. While such quantities can provide important insight into the underlying structure of these states and inform model calculations, defining and measuring such quantities experimentally present significant challenges. Experimentally the quantities of interest are the transition elements for the electroproduction processes $\gamma^* N \rightarrow N^*$, specifically the transverse and longitudinal helicity amplitudes $\mathcal{A}_{\frac{1}{2}}$ and $\mathcal{S}_{\frac{1}{2}}$.

Previous lattice calculations have focused primarily on the $\Delta \rightarrow N\gamma$ transition. The framework for such a calculation was established in Ref. [27] and subsequently examined comprehensively both in quenched [28, 29] and full QCD [30, 31]. For all of these studies, due to the choice of lattice ensemble parameters, the Δ baryon remains the lightest state in this channel and so this process can be examined using standard techniques. The results of [31] show good qualitative agreement with the experimental data, especially in the value extracted for $E2/M1$ ratio, however the authors outline that discrepancies observed in the exact behaviour of these amplitudes, particularly the $M1$ amplitude, highlight important chiral dynamics to this process.

The only other nucleon transition considered to date has been the $N^*(1440) \rightarrow N\gamma$ transition [32, 33]. However, as yet it is unlikely any group has properly isolated the $N^*(1440)$ on the lattice. The current understanding is that the $N^*(1440)$ Roper resonance is dynamically generated through rescattering in the πN , $\pi\Delta$, and σN channels [8, 10, 34], and significant advances on accessing multiparticle states in lattice QCD are being made [19, 20]. Experimental determinations indicate that the sign of the $\mathcal{A}_{\frac{1}{2}}$ transition form factor is negative at low Q^2 . This contrasts constituent quark models which predict a positive sign, lending further evidence the Roper resonance is not associated with a quark-model state. The need for at least three coupled meson-baryon channels to generate this resonance [10] presents a formidable challenge to first-principles lattice QCD calculations. However, evaluation of this amplitude will assist in understanding the underlying dynamics of the Roper resonance and the make up of this state, both on the lattice and in phenomenology.

A notably absent calculation is the evaluation of the odd-parity $N^*(1535) \rightarrow N\gamma$ transition. The focus of this work is the extraction of the transition form factors for such states. We begin with the presentation of a general framework through which one can determine $N^* \rightarrow N\gamma$ transition amplitudes for all choices and combinations of parity, all from the same baryon correlator. Then in the following section, we utilise this framework to examine the $\mathcal{A}_{\frac{1}{2}}$ and $\mathcal{S}_{\frac{1}{2}}$ form factors of the first two negative parity nucleon eigenstates.

Experimentally the quantities of interest are the transverse and longitudinal helicity amplitudes $\mathcal{A}_{\frac{1}{2}}$ and $\mathcal{S}_{\frac{1}{2}}$

$$\mathcal{A}_{\frac{1}{2}} = \sqrt{\frac{2\pi\alpha}{K}} \frac{1}{e} \langle N^*, s'_z = 1/2^+ | \epsilon_{\mu}^{(+)} J^{\mu} | N, s_z = 1/2^- \rangle, \quad (1)$$

$$\mathcal{S}_{\frac{1}{2}} = \sqrt{\frac{2\pi\alpha}{K}} \frac{1}{e} \frac{|\vec{q}|}{Q} \langle N^*, s'_z = 1/2^+ | \epsilon_{\mu}^{(0)} J^{\mu} | N, s_z = 1/2^+ \rangle, \quad (2)$$

where e is the magnitude of the electron's charge, α the electromagnetic fine structure constant and $Q = \sqrt{Q^2}$. Here ϵ_{μ} represents the polarisation of the incoming virtual photon, with $|\vec{q}|$ the photon's 3-momentum in the N^* rest frame and

$$K = \frac{M^2 - m^2}{2M}. \quad (3)$$

We identify M with the resonance N^* and m with the nucleon N . These amplitudes can in turn be related to matrix elements with the familiar form

$$\langle N^*, p', s' | J^{\mu} | N, p, s \rangle = e \left(\frac{M m}{E'(p') E(p)} \right)^{1/2} \bar{u}_{(M)}(p', s') \Gamma(p', p) u_{(m)}(p, s), \quad (4)$$

which parametrises the interaction in terms of Lorentz covariant structures. We note that all spinors in this and

subsequent expressions are regular Dirac spinors. Here the subscript, $u_{(\xi)}$, labels the mass of the state for which the spinor describes. A convenient choice of parametrisation is that first presented in Ref. [35] and nicely summarised in Refs. [36, 37], which allows us to express the normal-parity ($1/2^+ \rightarrow 1/2^+$) transition as

$$\langle N^*, p', s' | J^\mu | N, p, s \rangle = e \left(\frac{M m}{E'(\vec{p}') E(\vec{p})} \right)^{1/2} \bar{u}_{(M)}(p', s') \tilde{J}^\mu u_{(m)}(p, s), \quad (5)$$

and abnormal-parity ($1/2^+ \rightarrow 1/2^-$) transition

$$\langle N^*, p', s' | J^\mu | N, p, s \rangle = e \left(\frac{M m}{E'(\vec{p}') E(\vec{p})} \right)^{1/2} \bar{u}_{(M)}(p', s') \tilde{J}^\mu \gamma_5 u_{(m)}(p, s), \quad (6)$$

with

$$\tilde{J}^\mu = - [q^2 \gamma^\mu - \not{q} q^\mu] G_1(Q^2) - [(P \cdot q) \gamma^\mu - \not{P} P^\mu] G_2(Q^2), \quad (7)$$

and $P = \frac{1}{2}(p' + p)$.

Using this decomposition, the helicity amplitudes can be expressed in terms of G_1 and G_2 . For normal trans-

itions

$$\begin{aligned} \mathcal{A}_{\frac{1}{2}}^+(Q^2) &= \\ b_+ [2Q^2 G_1(Q^2) - (M^2 - m^2) G_2(Q^2)] , & \quad (8) \\ \mathcal{S}_{\frac{1}{2}}^+(Q^2) &= \end{aligned}$$

$$b_+ \frac{|\vec{q}|}{\sqrt{2}} [2(M + m) G_1(Q^2) + (M - m) G_2(Q^2)] , \quad (9)$$

and for abnormal transitions

$$\begin{aligned} \mathcal{A}_{\frac{1}{2}}^-(Q^2) &= \\ b_- [2Q^2 G_1(Q^2) - (M^2 - m^2) G_2(Q^2)] , & \quad (10) \\ \mathcal{S}_{\frac{1}{2}}^-(Q^2) &= \end{aligned}$$

$$b_- \frac{-|\vec{q}|}{\sqrt{2}} [2(M - m) G_1(Q^2) + (M + m) G_2(Q^2)] , \quad (11)$$

with

$$b_\pm = \sqrt{\frac{Q^2 + (M \mp m)^2}{8m(M^2 - m^2)}} , \quad (12)$$

Another popular choice of parametrisation is to express the vertex in terms of Pauli-Dirac-like form factors $F_1^*(Q^2)$ and $F_2^*(Q^2)$. Taking

$$F_1^*(Q^2) = Q^2 G_1(Q^2), \quad (13)$$

$$F_2^*(Q^2) = -\frac{(M^2 - m^2)}{2} G_2(Q^2), \quad (14)$$

one can re-express the transition matrix elements [37] as

$$\langle N_i^*, p', s' | J^\mu | N, p, s \rangle = e \left(\frac{M m}{E'(\vec{p}') E(\vec{p})} \right)^{1/2} \bar{u}_{(M)}(p', s') \Gamma_i^\mu(p', p) u_{(m)}(p, s), \quad (15)$$

where i denotes normal, n , or abnormal, a , transitions. For normal transitions

$$\Gamma_n^\mu(p', p) = \left(\delta_\nu^\mu - \frac{q_\nu q^\mu}{q^2} \right) \gamma^\nu F_1^*(Q^2) + \frac{i\sigma^{\mu\nu} q_\nu}{M + m} F_2^*(Q^2), \quad (16)$$

and for abnormal transitions

$$\Gamma_a^\mu(p', p) = \left(\delta_\nu^\mu - \frac{q_\nu q^\mu}{q^2} \right) \gamma^\nu \gamma_5 F_1^*(Q^2) + \frac{i\sigma^{\mu\nu} q_\nu}{M - m} \gamma_5 F_2^*(Q^2). \quad (17)$$

We note that our choice of normalisation for the F_2^* form factor in the abnormal transition vertex differs from the common choice [38, 39] by a factor of $\left(\frac{M-m}{M+m}\right)$. However, the absence of parity doubling in the low-lying energy eigenstates of QCD admit this formalism. The advantage of our normalisation is apparent if we consider the expressions for the helicity amplitudes in terms of the

Dirac- and Pauli-like form factors, namely

$$\mathcal{A}_{\frac{1}{2}}^\pm(Q^2) = 2b_\pm [F_1^*(Q^2) + F_2^*(Q^2)] , \quad (18)$$

$$\begin{aligned} \mathcal{S}_{\frac{1}{2}}^\pm(Q^2) &= \\ \pm \frac{\sqrt{2}b_\pm (M \pm m) |\vec{q}|}{Q^2} [F_1^*(Q^2) - \tau_\pm F_2^*(Q^2)] , & \quad (19) \end{aligned}$$

where b_{\pm} is defined in Eq. (12) and

$$\tau_{\pm} = \frac{Q^2}{(M \pm m)^2}, \quad (20)$$

with the \pm label indicating the parity of the resonant nucleon state. Hence, the helicity amplitudes are proportional to generalisations of the Sachs electric and magnetic form factors

$$G_E^*(Q^2) = F_1^*(Q^2) - \frac{Q^2}{(M \pm m)^2} F_2^*(Q^2), \quad (21)$$

$$G_M^*(Q^2) = F_1^*(Q^2) + F_2^*(Q^2). \quad (22)$$

Compare this to the choice of Refs. [38–40] where

$$F_2(Q^2) = \frac{M+m}{M-m} F_2^*(Q^2), \quad (23)$$

for the abnormal transition such that

$$\mathcal{A}_{\frac{1}{2}}^-(Q^2) = 2b_- \left[F_1^*(Q^2) + \frac{M-m}{M+m} F_2(Q^2) \right], \quad (24)$$

$$\begin{aligned} \mathcal{S}_{\frac{1}{2}}^-(Q^2) = & \\ & - \frac{\sqrt{2}b_- (M+m) |\vec{q}|}{Q^2} \left[\frac{M-m}{M+m} F_1^*(Q^2) - \tau_+ F_2(Q^2) \right]. \end{aligned} \quad (25)$$

In this case, the above identification with generalisations of the Sachs form factors is not possible due to a relative factor of $\left(\frac{M+m}{M-m}\right)$ between F_2^* and F_2 . In our analysis we shall use the decompositions given by Eqs. (16) and (17).

III. PARITY EXPANDED VARIATIONAL ANALYSIS

A. Two-point functions

The process of extracting transition form factors of baryonic excited states via the PEVA technique follows similarly to the elastic case presented in Ref [15]. We provide here a brief summary of this process and detail the generalisations required to handle transition matrix elements.

In this section we focus on a lattice QCD implementation of the formalism. We adopt the common Euclidean metric $\delta^{\mu\nu}$ and use the Hermitian Pauli representation for the Dirac matrices. With a Euclidean metric, there is no need to distinguish between contravariant and covariant indices.

We begin with a basis of n conventional spin-1/2 operators $\{\chi_i(x)\}$ that couple to the states of interest. We introduce the PEVA projector [14]

$$\Gamma_{\mp\mathbf{p}} \equiv \frac{1}{4} (\mathbb{I} + \gamma^4) (\mathbb{I} \mp i\gamma^5 \gamma^k \hat{\mathbf{p}}^k), \quad (26)$$

where there is an arbitrary sign choice in whether the unit vector $\hat{\mathbf{p}}$ is chosen to be parallel (+) or antiparallel

(−) to the momentum direction. This choice changes the sign of the cross-parity terms, but otherwise has no effect on the analysis of the two-point functions. However, as discussed later, it plays an important role in optimising the extraction of transition form factors for general kinematics. With this projector, a set of basis operators is constructed

$$\chi_{\mp\mathbf{p}i}(x) \equiv \Gamma_{\mp\mathbf{p}} \chi_i(x), \quad (27a)$$

$$\chi_{\mp\mathbf{p}i'}(x) \equiv \mp \Gamma_{\mp\mathbf{p}} \gamma^5 \chi_i(x). \quad (27b)$$

We then seek an optimised set of operators $\phi_{\mp\mathbf{p}}^{\alpha}(x)$ that each couple strongly to a single energy eigenstate α . These optimised operators are constructed as linear combinations of the basis operators. The optimum linear combinations are found by solving a generalised eigenvalue problem (GEVP) with $G(\mathbf{p}; t + \Delta t)$ and $G(\mathbf{p}; t)$, where the correlation matrix

$$\begin{aligned} G_{ij}(\mathbf{p}; t) & \\ & \equiv \text{Tr} \left(\sum_{\mathbf{x}} e^{-i\mathbf{p}\cdot\mathbf{x}} \langle \Omega | \chi_{\mp\mathbf{p}i}(x) \bar{\chi}_{\mp\mathbf{p}j}(0) | \Omega \rangle \right), \end{aligned} \quad (28)$$

with i and j ranging over both the primed and unprimed operators. This process is described in detail in Ref. [14].

Using the optimised operators, we can construct the eigenstate-projected two-point correlation function

$$\begin{aligned} G(\mathbf{p}; t; \alpha) & \\ & \equiv \text{Tr} \left(\sum_{\mathbf{x}} e^{-i\mathbf{p}\cdot\mathbf{x}} \langle \Omega | \phi_{\mp\mathbf{p}}^{\alpha}(x) \bar{\phi}_{\mp\mathbf{p}}^{\alpha}(0) | \Omega \rangle \right) \\ & = v_i^{\alpha}(\mathbf{p}) G_{ij}(\mathbf{p}; t) u_j^{\alpha}(\mathbf{p}). \end{aligned} \quad (29)$$

B. Three-point functions

The same approach is applied to lattice three-point correlation functions drawing on the eigenvectors obtained in solving the two-point GEVP

$$\begin{aligned} \mathcal{G}_{\mp}^3(\mathcal{J}; \mathbf{p}', \mathbf{p}; t_2, t_1; \alpha \rightarrow \beta) & \\ & \equiv \sum_{\mathbf{x}_1, \mathbf{x}_2} e^{-i\mathbf{p}'\cdot\mathbf{x}_2} e^{i(\mathbf{p}'-\mathbf{p})\cdot\mathbf{x}_1} \\ & \quad \times \langle \Omega | \phi_{\mp\mathbf{p}'}^{\beta}(x_2) \mathcal{J}(x_1) \bar{\phi}_{-\mathbf{p}}^{\alpha}(0) | \Omega \rangle, \end{aligned} \quad (30)$$

where $\mathcal{J}(x)$ is some current operator, which is inserted with a momentum transfer $\mathbf{q} = \mathbf{p}' - \mathbf{p}$. The consideration of $\mathcal{G}_{\mp}^3(\mathcal{J}; \mathbf{p}', \mathbf{p}; t_2, t_1; \alpha \rightarrow \beta)$ (where the sink operator uses the opposite PEVA projector sign convention to the source operator) is required to optimise the extraction of the form factors for general kinematics. We note that it is sufficient to consider this change of projector for the sink operator alone, leaving the source operator as $\bar{\phi}_{-\mathbf{p}}^{\alpha}(0)$ in all cases considered.

In this paper, we investigate electromagnetic transitions of the proton and neutron by choosing the current

operator $\mathcal{J}(x)$ to be the vector current. In particular, we use the $O(a)$ -improved [41] conserved vector current used in Ref. [42],

$$j_{CI}^\mu(x) \equiv j_C^\mu(x) + \frac{r}{2} a \bar{q}(x) \left(\overleftarrow{\nabla}^\rho + \overrightarrow{\nabla}^\rho \right) \sigma^{\rho\mu} q(x), \quad (31)$$

where r is the Wilson parameter, and $j_C^\mu(x)$ is the standard conserved vector current for the Wilson action, symmetrised about a lattice site.

As discussed in Section II, this choice of current operator gives the parity-conserving transition matrix element

$$\begin{aligned} \langle \beta^\pm; p'; s' | j_{CI}^\mu | \alpha^\pm; p; s \rangle &= \sqrt{\frac{m^\alpha}{E^\alpha(\mathbf{p})}} \sqrt{\frac{m^\beta}{E^\beta(\mathbf{p}')}} \bar{u}^\beta(p', s') \Gamma_n^\mu(p', p) u^\alpha(p, s) \\ &= \sqrt{\frac{m^\alpha}{E^\alpha(\mathbf{p})}} \sqrt{\frac{m^\beta}{E^\beta(\mathbf{p}')}} \bar{u}^\beta(p', s') \left(\left(\delta^{\mu\nu} - \frac{q^\mu q^\nu}{q^2} \right) \gamma^\nu F_1^*(Q^2) - \frac{\sigma^{\mu\nu} q^\nu}{m^\beta + m^\alpha} F_2^*(Q^2) \right) u^\alpha(p, s), \end{aligned} \quad (32)$$

where α and β have the same parity, and the parity-changing transition matrix element

$$\begin{aligned} \langle \beta^\mp; p'; s' | j_{CI}^\mu | \alpha^\pm; p; s \rangle &= \sqrt{\frac{m^\alpha}{E^\alpha(\mathbf{p})}} \sqrt{\frac{m^\beta}{E^\beta(\mathbf{p}')}} \bar{u}^\beta(p', s') \Gamma_a^\mu(p', p) u^\alpha(p, s) \\ &= \sqrt{\frac{m^\alpha}{E^\alpha(\mathbf{p})}} \sqrt{\frac{m^\beta}{E^\beta(\mathbf{p}')}} \bar{u}^\beta(p', s') \left(\left(\delta^{\mu\nu} - \frac{q^\mu q^\nu}{q^2} \right) \gamma^\nu \gamma^5 F_1^*(Q^2) - \frac{\sigma^{\mu\nu} q^\nu}{m^\beta - m^\alpha} \gamma^5 F_2^*(Q^2) \right) u^\alpha(p, s), \end{aligned} \quad (33)$$

where α and β have opposite parity. Note that these expressions differ from those in Section II due to conversion to the Pauli representation used in the current section. Here $Q^2 = \mathbf{q}^2 - (E^\alpha(\mathbf{p}') - E^\alpha(\mathbf{p}))^2$ is the squared four-momentum with the conventional sign, and the invariant scalar functions $F_1^*(Q^2)$ and $F_2^*(Q^2)$ are respectively the Dirac- and Pauli-like transition form factors defined in Equations 13 and 14.

To extract our desired signal from this spinor structure, we can take the spinor trace with some spin-structure projector Γ_S . This trace is then called the spinor-projected three-point correlation function

$$\begin{aligned} G_\mp^3(\Gamma_S; j_{CI}^\mu; \mathbf{p}', \mathbf{p}; t_2, t_1; \alpha \rightarrow \beta) &\equiv \text{Tr} \left[\Gamma_S G_\mp^3(j_{CI}^\mu; \mathbf{p}', \mathbf{p}; t_2, t_1; \alpha \rightarrow \beta) \right] \\ &= e^{-E^\beta(\mathbf{p}')(t_2-t_1)} e^{-E^\alpha(\mathbf{p})t_1} \frac{\bar{\mathcal{Z}}^\alpha(\mathbf{p})}{2E^\alpha(\mathbf{p})} \frac{\mathcal{Z}^\beta(\mathbf{p}')}{2E^\beta(\mathbf{p}')} \text{Tr} \left[\Gamma_S \Gamma_{\mp \mathbf{p}'} (\not{p} + m^\alpha) \Gamma_i^\mu(p, p') (\not{p}' + m^\beta) \Gamma_{-\mathbf{p}} \right], \end{aligned} \quad (34)$$

where the coefficients $\mathcal{Z}^\alpha(\mathbf{p})$ parametrise the operator overlaps

$$\langle \Omega | \phi_{\mp \mathbf{p}}^\alpha(0) | \alpha; p; s \rangle = \mathcal{Z}^\alpha(\mathbf{p}) \sqrt{\frac{m^\alpha}{E^\alpha(\mathbf{p})}} \Gamma_{\mp \mathbf{p}} u^\alpha(p, s). \quad (35)$$

These spinor-projected correlation functions have a nontrivial time dependence, which can be removed by constructing the ratio [43]

$$\begin{aligned} R_\mp^{\mu\nu}(\mathbf{p}', \mathbf{p}; \beta, \alpha) &\equiv \sqrt{\left| \frac{G_\mp^3(\Gamma^\nu; j_{CI}^\mu; \mathbf{p}', \mathbf{p}; t_2, t_1; \alpha \rightarrow \beta) G_\mp^3(\Gamma^\nu; j_{CI}^\mu; \mathbf{p}, \mathbf{p}'; t_2, t_1; \beta \rightarrow \alpha)}{G(\mathbf{p}'; t_2; \beta) G(\mathbf{p}; t_2; \alpha)} \right|} \\ &\times \text{sign}(G_\mp^3(\Gamma^\nu; j_{CI}^\mu; \mathbf{p}', \mathbf{p}; t_2, t_1; \alpha \rightarrow \beta)), \end{aligned} \quad (36)$$

where $\Gamma^4 = (\mathbb{I} + \gamma^4)/2$ and $\Gamma^k = (\mathbb{I} + \gamma^4)(i\gamma^5\gamma^k)/2$ form the basis for the spin projectors we use.

We can then define the reduced ratio

$$\begin{aligned} \bar{R}_\mp^{\mu\nu}(\mathbf{p}', \mathbf{p}; \beta, \alpha) &\equiv \sqrt{\frac{2E^\alpha(\mathbf{p})}{E^\alpha(\mathbf{p}) + m^\alpha}} \sqrt{\frac{2E^\beta(\mathbf{p}')}{E^\beta(\mathbf{p}') + m^\alpha}} R_\mp^{\mu\nu}(\mathbf{p}', \mathbf{p}; \beta, \alpha) \\ &= \text{Tr} \left[\Gamma^\nu \Gamma_{\mp \mathbf{p}'} \frac{\not{p} + m^\alpha}{E^\alpha(\mathbf{p}) + m^\alpha} \Gamma_i^\mu(p, p') \frac{\not{p}' + m^\beta}{E^\beta(\mathbf{p}') + m^\beta} \Gamma_{+\mathbf{p}} \right]. \end{aligned} \quad (37)$$

In order to isolate the form factors, we can express this trace (which is itself a linear combination of the form factors) as a matrix product

$$\bar{R}_{\mp}^{\mu\nu}(\mathbf{p}', \mathbf{p}; \beta, \alpha) = [K_{1,\mp}^{\mu\nu}(\mathbf{p}', \mathbf{p}; \beta, \alpha) \quad K_{2,\mp}^{\mu\nu}(\mathbf{p}', \mathbf{p}; \beta, \alpha)] \begin{bmatrix} F_1^*(Q^2) \\ F_2^*(Q^2) \end{bmatrix}, \quad (38)$$

expressed here in terms of the Pauli-Dirac decomposition.

The kinematic weights $K_{i,\mp}^{\mu\nu}(\mathbf{p}', \mathbf{p}; \beta, \alpha)$ are determined by substituting the explicit form for the vertex function in the trace and reducing the product of γ -matrices into expressions involving the incoming and outgoing energies and momenta, the eigenstate masses and the hadron spins via Pauli matrices. The evaluation of these expressions is presented in the Appendix. By expressing each independent determination of $\bar{R}_{\mp}^{\mu\nu}(\mathbf{p}', \mathbf{p}; \beta, \alpha)$ in this way, we can combine the results into a single vector equation

$$\mathbf{R} = \mathbb{K} \mathbf{F}, \quad (39)$$

where \mathbf{R} is a vector containing n independent ratio determinations, \mathbb{K} is an $n \times 2$ matrix of kinematic factors

and \mathbf{F} is a vector containing the 2 form factors. Provided we have at least two linearly independent determinations of $\bar{R}_{\alpha^i \rightarrow \beta^j}^{\mu\nu}(\mathbf{p}', \mathbf{p}; \Gamma', \Gamma; j, i)$, we can solve the linear system by taking the pseudo-inverse of \mathbb{K} via the Singular Value Decomposition (SVD) of \mathbb{K} , to give

$$\mathbf{F} = \mathbb{K}^+ \mathbf{R}. \quad (40)$$

To express this solution in terms of another choice of form factor decomposition, it is a simple matter of applying the relevant basis transformation matrix relating the two parametrisations. Consequently we can determine the generalised Sachs form factors and the helicity amplitudes through the following expressions,

$$\mathbf{G} = \begin{pmatrix} G_E^*(Q^2) \\ G_M^*(Q^2) \end{pmatrix} = \begin{pmatrix} 1 & -\frac{Q^2}{(M \pm m)^2} \\ 1 & 1 \end{pmatrix} \mathbb{K}^+ \mathbf{R} \quad (41)$$

$$\mathbf{H} = \begin{pmatrix} S_{\frac{1}{2}}(Q^2) \\ A_{\frac{1}{2}}(Q^2) \end{pmatrix} = b_{\pm} \begin{pmatrix} \pm \frac{\sqrt{2}(M \pm m)|\bar{q}|}{Q^2} & 0 \\ 0 & 2 \end{pmatrix} \begin{pmatrix} 1 & -\frac{Q^2}{(M \pm m)^2} \\ 1 & 1 \end{pmatrix} \mathbb{K}^+ \mathbf{R}. \quad (42)$$

IV. RESULTS

The results presented in this paper are calculated on the PACS-CS (2 + 1)-flavour full-QCD ensembles [44], made available through the ILDG [45]. These ensembles use a $32^3 \times 64$ lattice, and employ a renormalisation-group improved Iwasaki gauge action with $\beta = 1.90$ and non-perturbatively $O(a)$ -improved Wilson quarks, with $C_{SW} = 1.715$.

Our current study focuses on the matrix elements of low-lying energy eigenstates at larger quark masses where the states dominated by single-particle operators are the lowest-lying states in the finite-volume spectrum. Our aim is to implement the formalism established in the previous section and report the first *ab initio* calculation of the helicity amplitudes for electromagnetic transitions from the ground state nucleon to the first two odd-parity excitations.

The recent HEFT calculation of Ref. [13] indicates that the two odd-parity states observed on the lattice are the lowest states in the spectrum for the heaviest PACS-CS quark mass ensemble. Moreover, the HEFT analysis in-

dicates scattering state contaminations in the two-point correlation functions are well below 10% for this mass. Thus of the five PACS-CS ensembles, we select the ensemble with $m_{\pi} = 702$ MeV [44]. Given our phenomenological focus is on the quark model, we will consider this particular quark mass where the assumptions of the non-relativistic constituent quark model are best satisfied. We set the scale using the Sommer parameter with $r_0 = 0.4921(64)$ fm [44] providing $a = 0.1022(15)$ fm and $m_{\pi}^2 = 0.3884(113)$ GeV² based on 399 configurations.

For the variational analyses in this paper, we begin with the same eight-interpolator basis as in Refs. [1, 15], in which we studied the elastic form factors of the ground-state nucleon and three localised excitations. This basis is formed from the conventional spin- $\frac{1}{2}$ nucleon interpolators

$$\begin{aligned} \chi_1 &= \epsilon^{abc} [u^{a\top} (C\gamma^5) d^b] u^c, \text{ and} \\ \chi_2 &= \epsilon^{abc} [u^{a\top} (C) d^b] \gamma^5 u^c, \end{aligned} \quad (43)$$

with 16, 35, 100, or 200 sweeps of gauge-invariant Gaussian smearing [46] with a smearing fraction of $\alpha = 0.7$, applied at the quark source and sinks in creating the

propagators. For the PEVA analyses, this basis is expanded to sixteen operators as described in Section III. The gauge links used in the Gaussian smearing are first smoothed by applying four sweeps of three-dimensional isotropic stout-link smearing [47] with $\rho = 0.1$. Using this basis, the electromagnetic transitions between the ground state nucleon and the first two negative-parity excitations are examined.

To extract the transition form factors, we fix the source at time slice $N_t/4 = 16$ relative to a fixed boundary condition in time. Utilising the sequential source technique (SST) [48], we invert through the current, fixing the current insertion at time slice 21. We choose time slice 21 by inspecting the two point correlation functions associated with each state and observing that excited-state contaminations in the eigenstate-projected correlators are suppressed by time slice 21. This is evaluated by fitting the effective mass in this region to a single-state ansatz verifying that the full correlated χ^2/dof is satisfactory. We then extract the transition form factors as outlined in Section III for every possible sink time and once again look for a plateau consistent with the single-state ansatz.

When fitting correlators, the χ^2/dof is calculated with the full covariance matrix, and the χ^2 values of all fits are consistent with an appropriate χ^2 distribution. To avoid significant multi-particle contamination, we demand that our two- and three-point correlators are consistent with a single-state ansatz within the Euclidean time regions considered. As one proceeds to precision calculations of these transition form factors, it will be essential to examine the scattering-state contributions to the form factors in detail.

In performing the SST through the electromagnetic current insertion, one needs to commit to specific momentum insertions, \vec{q} . In quanta of $2\pi/L$ where L is the length of a side of the cubic volume, we select three values for \vec{q} including $(1, 0, 0)$, $(1, 1, 0)$ and $(2, 0, 0)$ for the three-momentum components. In the traditional fashion the final momentum of the state is projected by the Fourier transform of the three-point function, and the initial state momentum is inferred via momentum conservation. We consider several initial, \vec{p} , and final \vec{p}' momenta, with the intention of using boosts to access several momentum transfers [1, 15]. For each \vec{q} , we draw from permutations of $\vec{p} = (0, 0, 0)$, $(1, 0, 0)$, $(1, 1, 0)$, $(2, 0, 0)$, $(2, 1, 0)$, and $(3, 0, 0)$ with several momentum sign combinations as we aim to access space-like momentum transfers where $Q^2 = \vec{q}^2 - q_0^2$ is positive. To do so, we ensure the lower-lying nucleon ground state has the largest momentum between \vec{p} and \vec{p}' to minimise the difference $q_0 = p'_0 - p_0 = E' - E$ as the baryons are on-shell.

Of the space-like momentum-transfer combinations considered, four were found to generate good signal-to-noise correlation functions with excellent plateaus available for fitting. These momentum combinations are summarised in Table I. Using the masses of the ground-state nucleon, $m_0 = 1.429(09)$ GeV, the first excitation $m_1 = 1.996(25)$ GeV, and the second excitation

$m_2 = 2.010(39)$ GeV, and ensuring the lower-lying nucleon is assigned the larger momentum magnitudes, the associated Q^2 values for the transitions from states $0 \rightarrow 1$ and $0 \rightarrow 2$ are also reported in Table I.

Table I. The momenta considered in our three-point function analysis producing good signal-to-noise in the correlation functions at space-like momentum transfers. The initial three-momentum components, \vec{p} , the SST current momentum, \vec{q} , and the final momentum, \vec{p}' , are indicated in quanta of $2\pi/L$. To obtain space-like momentum transfers, the lower-lying nucleon is assigned the larger momentum magnitudes of \vec{p}' . Using the state masses provided in the text, Q^2 values are reported for the transitions from states $0 \rightarrow 1$ and $0 \rightarrow 2$.

\vec{p}	\vec{q}	\vec{p}'	$Q_{0 \rightarrow 1}^2$ / GeV	$Q_{0 \rightarrow 2}^2$ / GeV
0,0,0	1,1,0	1,1,0	0.066(24)	0.053(38)
1,0,0	1,1,0	2,1,0	0.150(18)	0.140(30)
-1,0,0	2,0,0	1,0,0	0.268(28)	0.253(44)
0,0,0	2,0,0	2,0,0	0.431(20)	0.420(31)

It's interesting to note that $\vec{q} = (1, 0, 0)$ is insufficient to generate space-like momentum transfers. The mass splitting between the states is significant and larger momentum differences are required to bring the state energies closer together.

As one might expect, when the excited state takes zero momentum, one obtains good signal to noise in the three-point correlation function. Another favourable momentum combination is when the momenta of the incoming and outgoing states differ by a sign. It's well known this type of Breit frame kinematics is favourable for form factors, and we now see it to be favourable in the case of transition form factors. The fourth favourable momentum combination in the second row of Table I is perhaps somewhat of a surprise. However, the three-momentum of the current insertion is the smallest available to generate space-like momentum transfer, and the magnitude of Q^2 is the second smallest of those considered.

In the next two subsections we examine the Pauli-Dirac form factors $F_1^*(Q^2)$ and $F_2^*(Q^2)$ for electromagnetic transitions from the ground-state nucleon to the first and second negative parity excitations. These form factors are defined in the covariant vertex function of Eq. (17) and used in Eq. (33). Subsequently, they will be related to the helicity amplitudes via the kinematic factors of Eq. (42). However, the fits to our correlation functions are performed for $F_1^*(Q^2)$ and $F_2^*(Q^2)$.

The form factors are obtained in the solution of Eq. (40) where the vector \mathbf{R} is constructed from the nontrivial components of the $4 \times 4 \times 2$ elements of $\bar{R}_{\mp}^{\mu\nu}(\mathbf{p}', \mathbf{p}; \beta, \alpha)$ defined in Eq. (37). We report contributions from the doubly-represented u -sector of the proton, u_p , and the singly-represented d -sector of the proton, d_p , individually. Each sector is reported for single quarks of unit charge such that the physical states are obtained

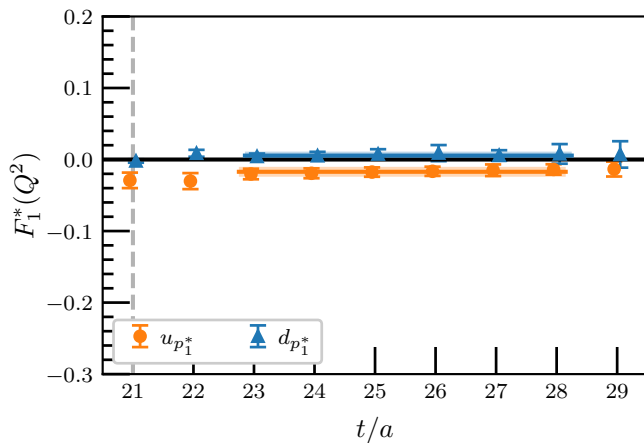


Figure 1. Quark-sector contributions to the three-point correlation function for the covariant vertex function $F_1^*(Q^2)$ at $Q^2 = 0.066(24)$ GeV² for the odd-parity transition between the ground state proton and the first negative-parity excitation. Sector contributions are normalised to represent single quarks of unit charge.

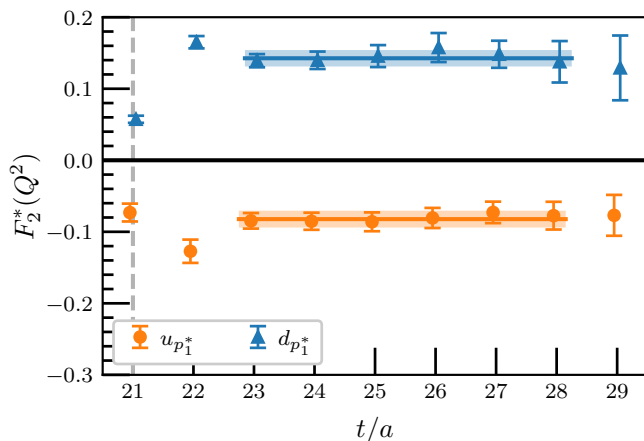


Figure 2. Quark-sector contributions to the three-point correlation function for the covariant vertex function $F_2^*(Q^2)$ at $Q^2 = 0.066(24)$ GeV² for the odd-parity transition between the ground state proton and the first negative-parity excitation. Sector contributions are normalised to represent single quarks of unit charge.

through simple quark counting and electric charge assignments. Schematically, the physical proton and neutron transition amplitudes are obtained via

$$p = \frac{2}{3} 2u_p - \frac{1}{3} d_p, \quad (44a)$$

$$n = -\frac{1}{3} 2u_p + \frac{2}{3} d_p. \quad (44b)$$

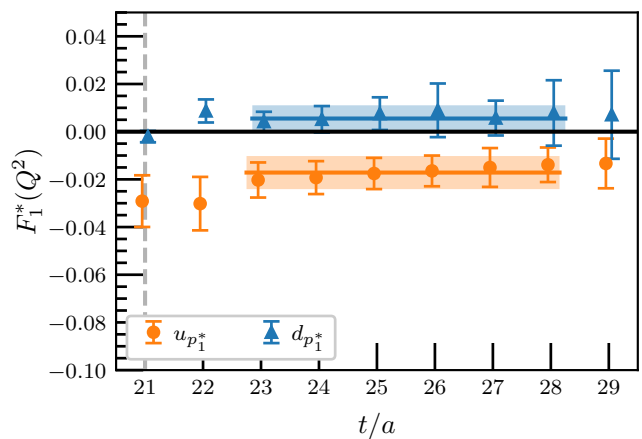


Figure 3. Zoomed-in presentation of the lattice QCD results presented in Fig. 1 for the transition between the ground state proton and the first negative-parity excitation. The onset of plateau behaviour is observed at two time steps following the current insertion at $t = 21$ and statistical uncertainties remain stable throughout the fit regime.

A. Transitions to the first negative parity excitation

Results for $F_1^*(Q^2)$ and $F_2^*(Q^2)$ in the odd parity electromagnetic transition for the ground-state proton to the first negative parity excitation are presented in Figs. 1 and 2 respectively. Here Q^2 takes the value 0.066(24) GeV², the lowest space-like momentum transfer available in this analysis. Values for F_1^* are small and a zoomed-in presentation of the fit is provided in Fig. 3.

The use of correlation matrix eigenvectors to aid in isolating the energy eigenstates leads to a rapid onset of plateau behaviour following the current insertion at $t = 21$. By two-time slices later, a persistent plateau is identified in the full covariance matrix fit.

It's interesting that for both form factors, the doubly-represented u sector of the proton contributes with a negative sign, while the singly-represented sector contributes with an opposite positive sign. In the dominant F_2^* form factor, the singly-represented d sector of the proton makes the largest contribution. Nevertheless, upon including quark-counting and charge factors, the doubly-represented u -quark sector of the proton will dominate, whereas the singly represented u -quark sector in the neutron will dominate.

With $F_1^*(Q^2)$ and $F_2^*(Q^2)$ determined in the correlation function ratio fits, we proceed to calculate the helicity amplitudes for the ground to first odd-parity excitation. Quark sectors are combined to create physical proton and neutron states via Eqs. (44) and the helicity amplitudes are obtained via Eq. (42). Figures 4 and 5 present the transverse and longitudinal helicity amplitudes respectively, as a function of the momentum transfer, Q^2 . Here our lattice QCD results at $m_\pi = 702$ MeV are presented in the context of constituent quark model pre-

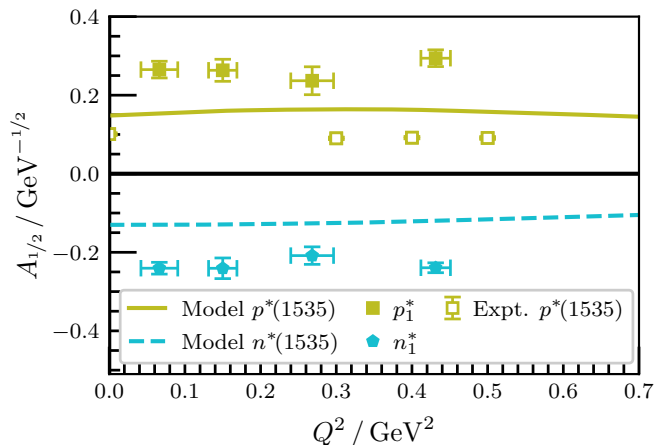


Figure 4. Transverse helicity amplitudes for transitions from the ground state nucleon to the first negative-parity excitation at $m_\pi = 702$ MeV (filled symbols) are presented in the context of results from a constituent quark model incorporating relativistic effects in a light-front framework [24] (lines) and experiment (open symbols).

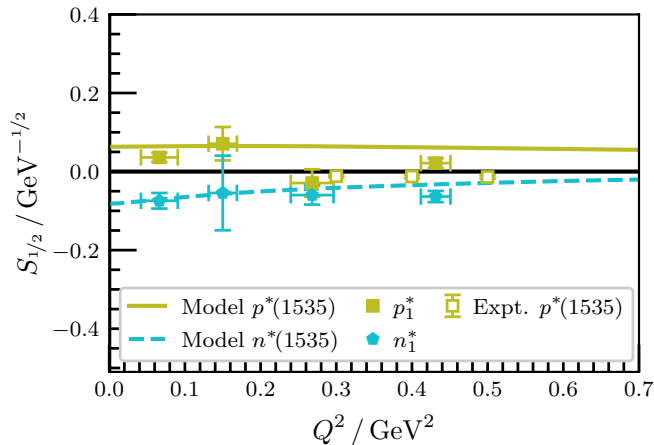


Figure 5. Longitudinal helicity amplitudes for transitions from the ground state nucleon to the first negative-parity excitation at $m_\pi = 702$ MeV (filled symbols) are presented in the context of results from a relativised constituent quark model [24] (lines) and experiment (open symbols).

dictions for the $N^*(1535)$ and experimental measurements. The quark model [24] incorporates relativistic effects in a light-front framework.

Our first observation for the transverse helicity amplitude is that the Q^2 dependence is very mild, a result reflected in both the constituent quark model and experiment. And while the sign of the proton and neutron helicity amplitudes are in accord with the model and available experimental results, the magnitude of our lattice results exceed both the model and experiment. It will be interesting to learn the relevant dynamics as one reduces the quark masses of the lattice QCD simulation toward the physical point. Assuming the lattice results approach the experimental measurements, it will be interesting to

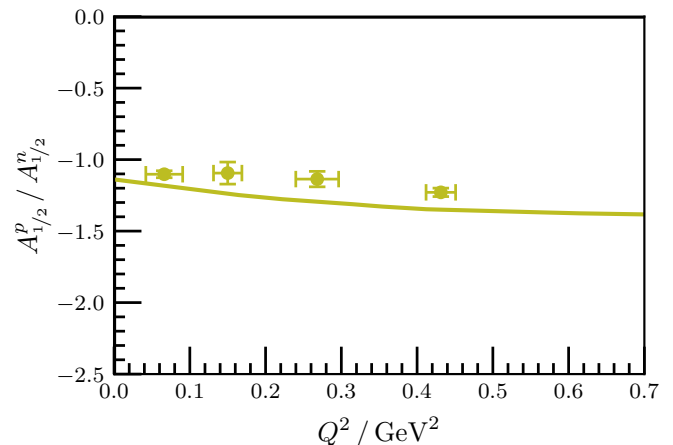


Figure 6. Ratio of proton to neutron transverse helicity amplitudes for transitions from the ground state to the first negative-parity excitation at $m_\pi = 702$ MeV (filled symbols) are compared with the relativised constituent quark model [24].

understand the relative roles of a simple quark mass dependence for each state contributing to the resonance amplitude and the resonance-related role of several finite-volume states contributing to the amplitude.

The longitudinal helicity amplitudes presented in Fig. 5 are relatively small. Here good agreement with the model results is observed for the excited proton at small Q^2 but the lattice QCD results do not show the Q^2 invariance of the model, instead dropping towards zero and even changing sign in accord with the experimental measurements. On the other hand, the lattice QCD results agree very well with the model results for the transition of the neutron to the $n^*(1535)$. Together, these results suggest that the quark mass dependence of this observable is likely to be mild.

It's interesting to examine the extent to which the lattice QCD and model predictions of the helicity amplitudes agree after the ratio of proton to neutron amplitudes are taken. In the ratio, quark mass effects have an opportunity to compensate, leaving a prediction more robust to quark mass variation. Figure 6 presents this ratio for the transverse helicity amplitude as a function of Q^2 . Again the trends match and the magnitudes are now quite similar.

B. Transitions to the second negative parity excitation

We now turn our attention to the electromagnetic transitions to the second low-lying negative-parity nucleon excitation observed on the lattice at $m_\pi = 702$ MeV and compare our results with quark model calculations of the $N^*(1650)$ and associated experimental measurements. It is here that the correlation matrix based eigenstate projection gains significant importance as we exam-

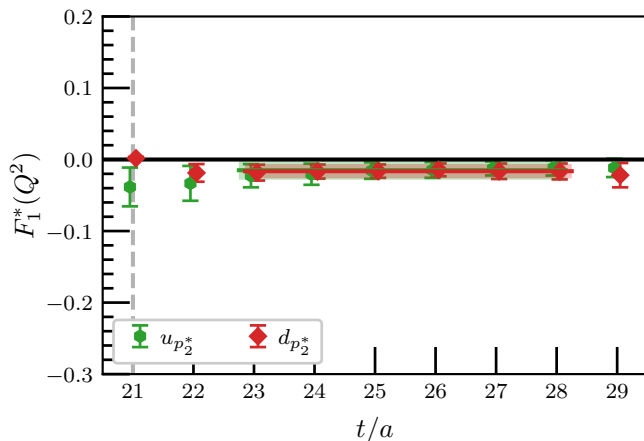


Figure 7. Quark-sector contributions to the three-point correlation function for the covariant vertex function $F_1^*(Q^2)$ at $Q^2 = 0.053(38)$ GeV^2 for the odd-parity transition between the ground state proton and the second negative-parity excitation. Sector contributions are normalised to represent single quarks of unit charge.

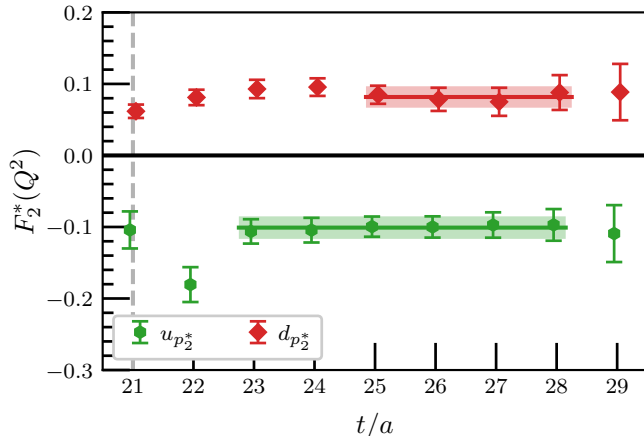


Figure 8. Quark-sector contributions to the three-point correlation function for the covariant vertex function $F_2^*(Q^2)$ at $Q^2 = 0.053(38)$ GeV^2 for the odd-parity transition between the ground state proton and the second negative-parity excitation. Sector contributions are normalised to represent single quarks of unit charge.

ine electromagnetic transitions to the second eigenstate in the odd-parity spectrum.

Results for $F_1^*(Q^2)$ and $F_2^*(Q^2)$ in the electromagnetic transition from the ground-state proton to the second negative parity excitation are presented in Figs. 7 and 8 respectively. Here the minimum space-like Q^2 takes a slightly smaller value of $0.053(38)$ GeV^2 due to the change in the mass of the excitation. Once again, values for F_1^* are small and a zoomed-in presentation of the fit is provided in Fig. 9. Here we observe slightly larger statistical uncertainties for the transition to the second odd-parity excitation.

The use of correlation-matrix eigenvector projection

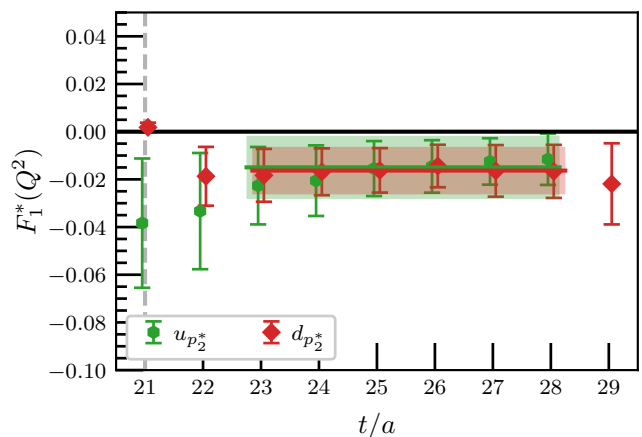


Figure 9. Zoomed-in presentation of the lattice QCD results presented in Fig. 7 for the transition between the ground state proton and the second negative-parity excitation. Statistical uncertainties are larger for this transition relative to the transition to the first negative-parity excitation illustrated in Fig. 3.

for state isolation leads to a rapid onset of plateau behaviour for three of the four correlators presented. Some fluctuation in the proton's singly-represented d -quark sector contribution to $F_2^*(Q^2)$ prevents an early fit due to uncomfortably large values for the full covariance matrix χ^2/dof .

This time there is a clear sign change between the contributions to $F_1^*(Q^2)$ and $F_2^*(Q^2)$ for the singly-represented d -quark sector in the proton. However, the doubly-represented u sector of the proton continues to uniformly contribute with a negative sign. In the dominant F_2^* form factor, both quark sectors make a contribution that is similar in magnitude. Upon including quark-counting and charge factors, the u -quark sector of the proton will dominate, whereas the sectors are more balanced for the neutron.

With $F_1^*(Q^2)$ and $F_2^*(Q^2)$ determined, we proceed to the helicity amplitudes for the ground to second odd-parity excitation. Figures 10 and 11 present the transverse and longitudinal helicity amplitudes respectively. Our lattice QCD results are presented in the context of the relativised constituent quark model [24] and experimental measurements where available.

A similar pattern of results for the transverse helicity amplitude is observed. Again, the Q^2 dependence is very mild in both the lattice and constituent quark model results. The signs of the proton and neutron helicity amplitudes from lattice QCD are in accord with the model and experiment. Again, the magnitude of our lattice results exceed both the model and experiment, suggesting an important quark mass dependence.

The longitudinal helicity amplitudes presented in Fig. 11 are relatively small. Reasonable agreement with the model results are observed. However, the sign of the experimental result at larger Q^2 differs. A high-statistics

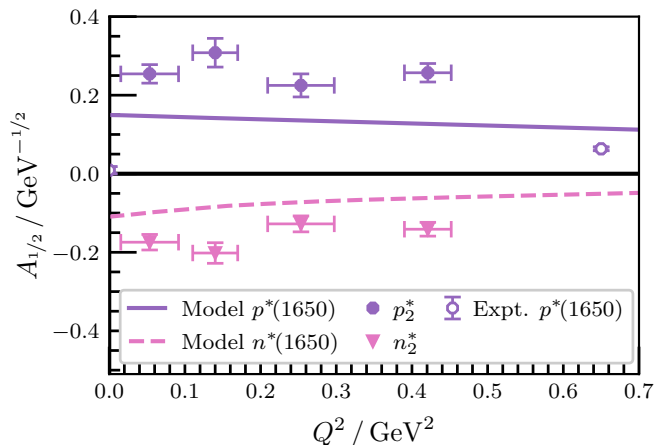


Figure 10. Transverse helicity amplitudes for transitions from the ground state nucleon to the second negative-parity excitation at $m_\pi = 702$ MeV (filled symbols) are presented in the context of results from a constituent quark model incorporating relativistic effects in a light-front framework [24] (lines) and experiment (open symbols).

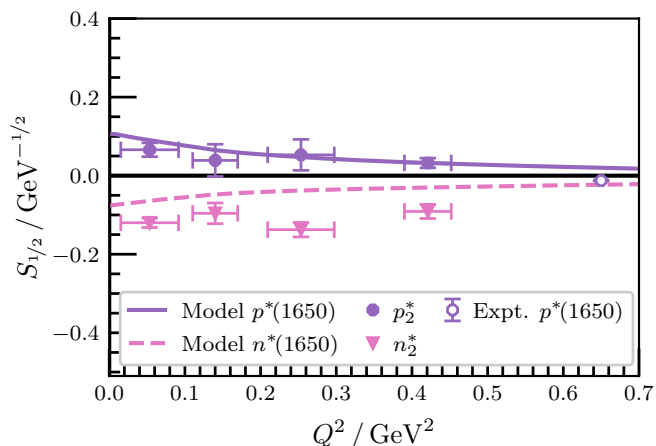


Figure 11. Longitudinal helicity amplitudes for transitions from the ground state nucleon to the second negative-parity excitation at $m_\pi = 702$ MeV (filled symbols) are presented in the context of results from a relativised constituent quark model [24] (lines) and experiment (open symbols).

analysis would be required to access this Q^2 , but such an analysis would be able to discern if the sign change is Q^2 related or quark-mass related.

On a final note, we examine the extent to which the lattice QCD and model predictions of the transverse helicity amplitudes agree after the ratio of proton to neutron amplitudes are taken to make a comparison more robust to quark mass variation. Figure 12 illustrates matching Q^2 trends with comparable magnitudes in the ratio.

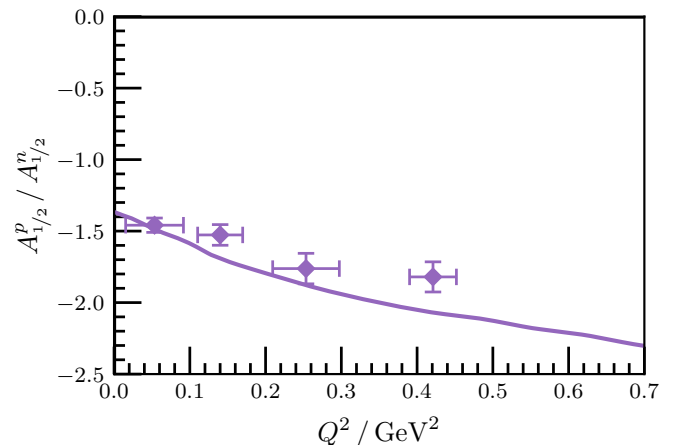


Figure 12. Ratio of proton to neutron transverse helicity amplitudes for transitions from the ground state to the second negative-parity excitation at $m_\pi = 702$ MeV (filled symbols) are compared with the relativised constituent quark model [24].

V. CONCLUSION

A formalism for the determination of spin-1/2 electromagnetic transition form factors in lattice QCD has been established. Both normal parity-conserving transitions and abnormal parity-changing transitions have been included in our considerations. After working with the standard covariant vertex functions, we introduce a new set of covariant vertex functions which more closely resemble the Pauli-Dirac elastic form factors.

Using the parity-expanded variational analysis (PEVA) technique [1, 14, 15], the new formalism is implemented in the first lattice QCD calculation of the helicity amplitudes for transitions from the ground state nucleon to both the first and the second odd-parity excitations observed in lattice QCD at $m_\pi = 702$ MeV. The selection of a large pion mass avoids significant complications associated with the mixing with two-particle states to become scattering states.

Statistical uncertainties in the transition form factors are found to be similar for both states, with only slightly larger fluctuations in the Pauli-Dirac form factor $F_1^*(Q^2)$ and slightly larger statistical uncertainties in $F_2^*(Q^2)$ for the second odd-parity excitation of the nucleon.

Our lattice QCD results are compared comprehensively with a relativised constituent quark model using a light-front formalism [24]. In every case, the lattice QCD results for the transverse and longitudinal helicity amplitudes agree with the quark model in sign. This includes both proton and neutron amplitudes and electromagnetic transitions to both the first and the second excitation. Moreover, when a ratio of proton to neutron results is considered to suppress quark-mass related effects, the results compare favourably.

Combined with our earlier results favourably comparing lattice QCD and the quark model for the electromag-

netic form factors of these odd-parity excitations, the results presented here provide further credence that the two low-lying odd-parity excitations of the nucleon observed in experiment are associated with quark-model like basis states which are dressed to form resonances.

The magnitude of the lattice QCD results for the transverse helicity amplitudes are larger than that predicted by the quark model as it was tuned to describe experiment. Indeed, the experimental measurements are even smaller than that predicted by the quark model. Together, these hint at a quark mass effect that is significant for the transverse helicity amplitude. It will be interesting to learn the relevant dynamics as one reduces the quark masses of the lattice QCD simulation toward the physical point. While the predominant effect may be a simple quark-mass dependence for each state contributing to the resonance amplitude, effects from combin-

ing the contributions from several finite-volume states to form the resonance are a novel possibility.

Thus working towards the physical quark-mass requires the introduction of multi-particle interpolating fields that will mix with the single-particle interpolators considered herein [13]. In the three-point function calculation, one will need to perform current insertions on all five of the quark propagators, further increasing the demands of the calculation. As the bare quark-model-like basis state mixes with the nearby two-particle states its contribution will be spread over several finite-volume states. It will be fascinating to learn the transition amplitudes to each of these finite-volume states and how they differ. Finally, it will be important to probe larger space-like Q^2 values to make direct confrontations with experimental measurements.

Appendix: Kinematic factors

As discussed in Section IIIB, the reduced ratio $\bar{R}_{\mp}^{\mu\nu}(\mathbf{p}', \mathbf{p}; \beta, \alpha)$ can be expressed as a matrix product

$$\bar{R}_{\mp}^{\mu\nu}(\mathbf{p}', \mathbf{p}; \beta, \alpha) = [K_{1,\mp}^{\mu\nu}(\mathbf{p}', \mathbf{p}; \beta, \alpha) \quad K_{2,\mp}^{\mu\nu}(\mathbf{p}', \mathbf{p}; \beta, \alpha)] \begin{bmatrix} F_{1\mp}^*(Q^2) \\ F_{2\mp}^*(Q^2) \end{bmatrix}, \quad (\text{A.1})$$

of some kinematic weights $K_{i,\pm}^{\mu\nu}(\mathbf{p}', \mathbf{p}; \beta, \alpha)$ and the Pauli-Dirac-like form factors, $F_{1\mp}^*(Q^2)$ and $F_{2\mp}^*(Q^2)$. These kinematic factors can be obtained by evaluating traces of the form

$$F'_{\mp}(\Gamma, \mathcal{J}) \equiv 8EE' \text{Tr} \left(\Gamma \Gamma_{\mp \mathbf{p}'} \frac{-i\gamma \cdot \mathbf{p}' + \mathbb{I}M'}{2E'} \mathcal{J} \frac{-i\gamma \cdot \mathbf{p} + \mathbb{I}M}{2E} \Gamma_{-\mathbf{p}} \right). \quad (\text{A.2})$$

Specifically, in the Pauli representation, for normal, parity-conserving transitions,

$$K_{1,\mp,n}^{\mu\nu}(\mathbf{p}', \mathbf{p}; \beta, \alpha) = \left(\delta^{\mu\rho} - \frac{q^\mu q^\rho}{q^2} \right) F'_{\mp}(\Gamma^\nu, \gamma^\rho) \quad \text{and} \quad (\text{A.3})$$

$$K_{2,\mp,n}^{\mu\nu}(\mathbf{p}', \mathbf{p}; \beta, \alpha) = -\frac{q^\rho}{m^\beta + m^\alpha} F'_{\mp}(\Gamma^\nu, \sigma^{\mu\rho}), \quad (\text{A.4})$$

and for abnormal, parity-changing transitions

$$K_{1,\mp,a}^{\mu\nu}(\mathbf{p}', \mathbf{p}; \beta, \alpha) = \left(\delta^{\mu\rho} - \frac{q^\mu q^\rho}{q^2} \right) F'_{\mp}(\Gamma^\nu, \gamma^\rho \gamma^5) \quad \text{and} \quad (\text{A.5})$$

$$K_{2,\mp,a}^{\mu\nu}(\mathbf{p}', \mathbf{p}; \beta, \alpha) = -\frac{q^\rho}{m^\beta - m^\alpha} F'_{\mp}(\Gamma^\nu, \sigma^{\mu\rho} \gamma^5). \quad (\text{A.6})$$

These traces were evaluated in the Pauli representation in Ref. [49], and are reproduced below for completeness:

$$\begin{aligned} F'_{\mp}(\Gamma^4, \mathbb{I}) &= ((E+m)(E'+m') \mp |\mathbf{p}||\mathbf{p}'|) (1 \pm \hat{p}^i \hat{p}'^i) \\ F'_{\mp}(\Gamma^4, \gamma^i) &= -(|\mathbf{p}|(E'+m') \pm |\mathbf{p}'|(E+m)) (\pm \epsilon^{ijk} \hat{p}^j \hat{p}'^k + i(\hat{p}^i \pm \hat{p}'^i)) \\ F'_{\mp}(\Gamma^4, \gamma^4) &= ((E+m)(E'+m') \pm |\mathbf{p}||\mathbf{p}'|) (1 \pm \hat{p}^i \hat{p}'^i) \\ F'_{\mp}(\Gamma^4, \gamma^5) &= (|\mathbf{p}|(E'+m') \mp |\mathbf{p}'|(E+m)) (1 \pm \hat{p}^i \hat{p}'^i) \\ F'_{\mp}(\Gamma^4, \gamma^i \gamma^5) &= -((E+m)(E'+m') \pm |\mathbf{p}||\mathbf{p}'|) (\pm \epsilon^{ijk} \hat{p}^j \hat{p}'^k + i(\hat{p}^i \pm \hat{p}'^i)) \\ F'_{\mp}(\Gamma^4, \gamma^4 \gamma^5) &= (|\mathbf{p}|(E'+m') \pm |\mathbf{p}'|(E+m)) (1 \pm \hat{p}^i \hat{p}'^i) \\ F'_{\mp}(\Gamma^4, \sigma^{4i}) &= i(|\mathbf{p}|(E'+m') \mp |\mathbf{p}'|(E+m)) (\pm \epsilon^{ijk} \hat{p}^j \hat{p}'^k + i(\hat{p}^i \pm \hat{p}'^i)) \end{aligned}$$

$$\begin{aligned}
F'_{\mp}(\Gamma^4, \sigma^{ij}) &= -((E+m)(E'+m') \mp |\mathbf{p}||\mathbf{p}'|) (\epsilon^{ijk} (\hat{p}^k \pm \hat{p}'^k) \mp i (\hat{p}^i \hat{p}'^j - \hat{p}^j \hat{p}'^i)) \\
F'_{\mp}(\Gamma^k, \mathbb{1}) &= -i((E+m)(E'+m') \mp |\mathbf{p}||\mathbf{p}'|) (\pm \epsilon^{ijk} \hat{p}^j \hat{p}'^k - i (\hat{p}^i \pm \hat{p}'^i)) \\
F'_{\mp}(\Gamma^k, \gamma^j) &= i(|\mathbf{p}|(E'+m') \pm |\mathbf{p}'|(E+m)) \\
&\quad \times (\pm \hat{p}^i \hat{p}'^j \pm \hat{p}^j \hat{p}'^i - i \epsilon^{ijk} (\hat{p}^k \mp \hat{p}'^k) + \delta^{ij} (1 \mp \hat{p}^k \hat{p}'^k)) \\
F'_{\mp}(\Gamma^k, \gamma^4) &= -i((E+m)(E'+m') \pm |\mathbf{p}||\mathbf{p}'|) (\pm \epsilon^{ijk} \hat{p}^j \hat{p}'^k - i (\hat{p}^i \pm \hat{p}'^i)) \\
F'_{\mp}(\Gamma^k, \gamma^5) &= -i(|\mathbf{p}|(E'+m') \mp |\mathbf{p}'|(E+m)) (\pm \epsilon^{ijk} \hat{p}^j \hat{p}'^k - i (\hat{p}^i \pm \hat{p}'^i)) \\
F'_{\mp}(\Gamma^k, \gamma^j \gamma^5) &= i((E+m)(E'+m') \pm |\mathbf{p}||\mathbf{p}'|) \\
&\quad \times (\pm \hat{p}^i \hat{p}'^j \pm \hat{p}^j \hat{p}'^i - i \epsilon^{ijk} (\hat{p}^k \mp \hat{p}'^k) + \delta^{ij} (1 \mp \hat{p}^k \hat{p}'^k)) \\
F'_{\mp}(\Gamma^k, \gamma^4 \gamma^5) &= -i(|\mathbf{p}|(E'+m') \pm |\mathbf{p}'|(E+m)) (\pm \epsilon^{ijk} \hat{p}^j \hat{p}'^k - i (\hat{p}^i \pm \hat{p}'^i)) \\
F'_{\mp}(\Gamma^k, \sigma^{4j}) &= (|\mathbf{p}|(E'+m') \mp |\mathbf{p}'|(E+m)) \\
&\quad \times (\pm \hat{p}^i \hat{p}'^j \pm \hat{p}^j \hat{p}'^i - i \epsilon^{ijk} (\hat{p}^k \mp \hat{p}'^k) + \delta^{ij} (1 \mp \hat{p}^k \hat{p}'^k)) \\
F'_{\mp}(\Gamma^k, \sigma^{jk}) &= ((E+m)(E'+m') \mp |\mathbf{p}||\mathbf{p}'|) \epsilon^{jkl} \\
&\quad \times (\pm \hat{p}^i \hat{p}'^l \pm \hat{p}^l \hat{p}'^i - i \epsilon^{ilm} (\hat{p}^m \mp \hat{p}'^m) + \delta^{il} (1 \mp \hat{p}^m \hat{p}'^m))
\end{aligned}$$

ACKNOWLEDGMENTS

We thank the PACS-CS Collaboration for making their configurations available via the International Lattice Data Grid (ILDG). This research was undertaken with the assistance of resources from the Phoenix HPC service at the University of Adelaide, the National Computational Infrastructure (NCI), which is supported by the Australian Government, and by resources provided by the Pawsey Supercomputing Centre with funding from the Australian Government and the Government of West-

ern Australia. These resources were provided through the National Computational Merit Allocation Scheme and the University of Adelaide partner share. FS is supported by a Ramsay Fellowship from the University of Adelaide. WK was supported by the Pawsey Supercomputing Centre through the Pawsey Centre for Extreme Scale Readiness (PaCER) program. This research is supported by the Australian Research Council through grants no. DP140103067, DP150103164, LE160100051, LE190100021, DP190102215, and DP210103706.

-
- [1] F. M. Stokes, W. Kamleh, and D. B. Leinweber, Phys. Rev. D **102**, 014507 (2020), arXiv:1907.00177 [hep-lat].
- [2] W.-T. Chiang, S. N. Yang, M. Vanderhaeghen, and D. Drechsel, Nucl. Phys. **A723**, 205 (2003), arXiv:nucl-th/0211061 [nucl-th].
- [3] J. Liu, J. He, and Y. B. Dong, Phys. Rev. **D71**, 094004 (2005).
- [4] N. Sharma, A. Martinez Torres, K. P. Khemchandani, and H. Dahiya, Eur. Phys. J. **A49**, 11 (2013), arXiv:1207.3311 [hep-ph].
- [5] J. M. M. Hall, A. C. P. Hsu, D. B. Leinweber, A. W. Thomas, and R. D. Young, Phys. Rev. D **87**, 094510 (2013), arXiv:1303.4157 [hep-lat].
- [6] J. M. M. Hall, W. Kamleh, D. B. Leinweber, B. J. Menadue, B. J. Owen, A. W. Thomas, and R. D. Young, Phys. Rev. Lett. **114**, 132002 (2015), arXiv:1411.3402 [hep-lat].
- [7] Z.-W. Liu, W. Kamleh, D. B. Leinweber, F. M. Stokes, A. W. Thomas, and J.-J. Wu, Phys. Rev. Lett. **116**, 082004 (2016), arXiv:1512.00140 [hep-lat].
- [8] Z.-W. Liu, W. Kamleh, D. B. Leinweber, F. M. Stokes, A. W. Thomas, and J.-J. Wu, Phys. Rev. D **95**, 034034 (2017), arXiv:1607.04536 [nucl-th].
- [9] Z.-W. Liu, J. M. M. Hall, D. B. Leinweber, A. W. Thomas, and J.-J. Wu, Phys. Rev. D **95**, 014506 (2017), arXiv:1607.05856 [nucl-th].
- [10] J.-j. Wu, D. B. Leinweber, Z.-w. Liu, and A. W. Thomas, Phys. Rev. D **97**, 094509 (2018), arXiv:1703.10715 [nucl-th].
- [11] C. D. Abell, D. B. Leinweber, A. W. Thomas, and J.-J. Wu, Phys. Rev. D **106**, 034506 (2022), arXiv:2110.14113 [hep-lat].
- [12] C. D. Abell, D. B. Leinweber, A. W. Thomas, and J.-J. Wu, Annals Phys. **459**, 169531 (2023), arXiv:2305.18790 [nucl-th].
- [13] C. D. Abell, D. B. Leinweber, Z.-W. Liu, A. W. Thomas, and J.-J. Wu, Phys. Rev. D **108**, 094519 (2023), arXiv:2306.00337 [hep-lat].
- [14] F. M. Stokes, W. Kamleh, D. B. Leinweber, M. S. Mahbub, B. J. Menadue, and B. J. Owen, Phys. Rev. D **92**, 114506 (2015), arXiv:1302.4152 [hep-lat].
- [15] F. M. Stokes, W. Kamleh, and D. B. Leinweber, Phys. Rev. D **99**, 074506 (2019), arXiv:1809.11002 [hep-lat].
- [16] C. B. Lang and V. Verduci, Phys. Rev. D **87**, 054502 (2013), arXiv:1212.5055 [hep-lat].
- [17] C. W. Andersen, J. Bulava, B. Hörz, and C. Morningstar, Phys. Rev. D **97**, 014506 (2018), arXiv:1710.01557 [hep-lat].

- [18] G. Silvi *et al.*, Phys. Rev. D **103**, 094508 (2021), arXiv:2101.00689 [hep-lat].
- [19] C. Morningstar, J. Bulava, A. D. Hanlon, B. Hörz, D. Mohler, A. Nicholson, S. Skinner, and A. Walker-Loud, PoS **LATTICE2021**, 170 (2022), arXiv:2111.07755 [hep-lat].
- [20] J. Bulava, A. D. Hanlon, B. Hörz, C. Morningstar, A. Nicholson, F. Romero-López, S. Skinner, P. Vranas, and A. Walker-Loud, Nucl. Phys. B **987**, 116105 (2023), arXiv:2208.03867 [hep-lat].
- [21] J. Bulava *et al.* (Baryon Scattering (BaSc)), Phys. Rev. Lett. **132**, 051901 (2024), arXiv:2307.10413 [hep-lat].
- [22] J. Bulava *et al.* (Baryon Scattering (BaSc)), Phys. Rev. D **109**, 014511 (2024), arXiv:2307.13471 [hep-lat].
- [23] J. Bulava *et al.*, in *20th International Conference on Hadron Spectroscopy and Structure* (2023) arXiv:2310.08375 [hep-lat].
- [24] S. Capstick and B. D. Keister, Phys. Rev. D **51**, 3598 (1995), arXiv:nucl-th/9411016.
- [25] C. Michael, Nucl. Phys. B **259**, 58 (1985).
- [26] M. Luscher and U. Wolff, Nucl. Phys. B **339**, 222 (1990).
- [27] D. B. Leinweber, T. Draper, and R. M. Woloshyn, Phys. Rev. D **48**, 2230 (1993), arXiv:hep-lat/9212016.
- [28] C. Alexandrou, P. de Forcrand, T. Lippert, H. Neff, J. W. Negele, K. Schilling, W. Schroers, and A. Tsapalis, Phys. Rev. D **69**, 114506 (2004), arXiv:hep-lat/0307018.
- [29] C. Alexandrou, P. de Forcrand, H. Neff, J. W. Negele, W. Schroers, and A. Tsapalis, Phys. Rev. Lett. **94**, 021601 (2005), arXiv:hep-lat/0409122.
- [30] C. Alexandrou, G. Koutsou, H. Neff, J. W. Negele, W. Schroers, and A. Tsapalis, Phys. Rev. D **77**, 085012 (2008), arXiv:0710.4621 [hep-lat].
- [31] C. Alexandrou, G. Koutsou, J. W. Negele, Y. Proestos, and A. Tsapalis, Phys. Rev. D **83**, 014501 (2011), arXiv:1011.3233 [hep-lat].
- [32] H.-W. Lin, S. D. Cohen, R. G. Edwards, and D. G. Richards, Phys. Rev. D **78**, 114508 (2008), arXiv:0803.3020 [hep-lat].
- [33] H.-W. Lin and S. D. Cohen, AIP Conf. Proc. **1432**, 305 (2012), arXiv:1108.2528 [hep-lat].
- [34] D. B. Leinweber, C. D. Abell, L. C. Hockley, W. Kamleh, Z.-W. Liu, F. M. Stokes, A. W. Thomas, and J.-J. Wu, in *20th International Conference on Hadron Spectroscopy and Structure* (2024) arXiv:2401.04901 [hep-lat].
- [35] R. C. E. Devenish, T. S. Eizenschitz, and J. G. Korner, Phys. Rev. D **14**, 3063 (1976).
- [36] I. G. Aznauryan, V. D. Burkert, and T. S. H. Lee, (2008), arXiv:0810.0997 [nucl-th].
- [37] I. G. Aznauryan and V. D. Burkert, Prog. Part. Nucl. Phys. **67**, 1 (2012), arXiv:1109.1720 [hep-ph].
- [38] G. Ramalho and M. T. Pena, Phys. Rev. D **84**, 033007 (2011), arXiv:1105.2223 [hep-ph].
- [39] G. Ramalho and K. Tsushima, Phys. Rev. D **84**, 051301 (2011), arXiv:1105.2484 [hep-ph].
- [40] G. Ramalho and M. T. Peña, Prog. Part. Nucl. Phys. **136**, 104097 (2024), arXiv:2306.13900 [hep-ph].
- [41] G. Martinelli, C. T. Sachrajda, and A. Vladikas, Nucl. Phys. B **358**, 212 (1991).
- [42] S. Boinepalli, D. B. Leinweber, A. G. Williams, J. M. Zanotti, and J. B. Zhang, Phys. Rev. D **74**, 093005 (2006), arXiv:hep-lat/0604022.
- [43] D. B. Leinweber, R. M. Woloshyn, and T. Draper, Phys. Rev. D **43**, 1659 (1991).
- [44] S. Aoki *et al.* (PACS-CS), Phys. Rev. D **79**, 034503 (2009), arXiv:0807.1661 [hep-lat].
- [45] M. G. Beckett, B. Joo, C. M. Maynard, D. Pleiter, O. Tatebe, and T. Yoshie, Comput. Phys. Commun. **182**, 1208 (2011), arXiv:0910.1692 [hep-lat].
- [46] S. Gusken, Nucl. Phys. B Proc. Suppl. **17**, 361 (1990).
- [47] C. Morningstar and M. J. Peardon, Phys. Rev. D **69**, 054501 (2004), arXiv:hep-lat/0311018.
- [48] C. W. Bernard, T. Draper, G. Hockney, and A. Soni, in *Workshop on Lattice Gauge Theories* (1985).
- [49] F. M. Stokes, *Structure of Nucleon Excited States from Lattice QCD*, Ph.D. thesis, Adelaide U., Sch. Chem. Phys. (2019).